

Internal shear layers from librating objects

Stéphane Le Dizès^{1,†} and Michael Le Bars¹

¹CNRS, Aix Marseille Univ, Centrale Marseille, IRPHE, F-13013 Marseille, France

(Received 31 March 2017; revised 8 June 2017; accepted 4 July 2017)

In this work, we analyse the internal shear layer structures generated by the libration of an axisymmetric object in an unbounded fluid rotating at a rotation rate Ω^* using direct numerical simulation and small Ekman number asymptotic analysis. We consider weak libration amplitude and libration frequency ω^* within the inertial wave interval $(0, 2\Omega^*)$ such that the fluid dynamics is mainly described by a linear axisymmetric harmonic solution. The internal shear layer structures appear along the characteristic cones of angle $\theta_c = \text{acos}(\omega^*/(2\Omega^*))$ which are tangent to the librating object at so-called critical latitudes. These layers correspond to thin viscous regions where the singularities of the inviscid solution are smoothed. We assume that the velocity field in these layers is described by the class of similarity solutions introduced by Moore & Saffman (*Phil. Trans. R. Soc. Lond. A*, vol. 264, 1969, pp. 597–634). These solutions are characterized by two parameters only: a real parameter m , which measures the strength of the underlying singularity, and a complex amplitude coefficient C_0 . We first analyse the case of a disk for which a general asymptotic solution for small Ekman numbers is known when the disk is in a solid plane. We demonstrate that the numerical solutions obtained for a free disk and for a disk in a solid plane are both well described by the asymptotic solution and by its similarity form within the internal shear layers. For the disk, we obtain a parameter $m = 1$ corresponding to a Dirac source at the edge of the disk and a coefficient $C_0 \propto E^{1/6}$ where E is the Ekman number. The case of a smoothed librating object such as a spheroid is found to be different. By asymptotically matching the boundary layer solution to similarity solutions close to a critical latitude on the surface, we show that the adequate parameter m for the similarity solution is $m = 5/4$, leading to a coefficient $C_0 \propto E^{1/12}$, that is larger than for the case of a disk for small Ekman numbers. A simple general expression for C_0 valid for any axisymmetric object is obtained as a function of the local curvature radius at the critical latitude in agreement with this change of scaling. This result is tested and validated against direct numerical simulations.

Key words: boundary layer separation, waves in rotating fluids

1. Introduction

In a rotating fluid, localized time-harmonic perturbations propagate if their frequency ω^* is smaller than twice the fluid rotation rate Ω^* (Greenspan 1968). The propagation occurs along conical surfaces of angle $\theta_c = \text{acos}(\omega^*/(2\Omega^*))$ with

† Email address for correspondence: ledizes@irphe.univ-mrs.fr

respect to the plane normal to the rotation axis. Oscillating singularities travel within the fluid the same way. When these singular surfaces are smoothed by viscosity, they form internal shear layers. The goal of the present work is to analyse the structure and the amplitude of such layers when they are created by the (longitudinal) libration of an axisymmetric object in an open domain.

Longitudinal libration denotes harmonic oscillation of the rotation rate without modification of the rotation axis. It constitutes one of the possible harmonic forcings in planetology. Other forcings such as tide, precession, latitudinal libration are also present in most gravitational systems (Le Bars, Cébron & Le Gal 2015). Longitudinal libration is especially important for so-called synchronized bodies, i.e. bodies locked with their main companion in a given spin-orbit resonance, which is periodically perturbed by gravitational interactions with other bodies. This includes moons and small planets of our solar system, as well as some of the detected exoplanets in extra-solar systems, which orbit close to their star (see e.g. discussion in Cébron *et al.* 2012). The observed responses of those bodies to libration forcing, and more specifically the small changes in the measured spin rate of their surfaces, are used to remotely investigate their internal composition, showing for instance the presence of a liquid core in Mercury (Margot *et al.* 2007) and of a global subsurface ocean in Enceladus (Thomas *et al.* 2016). Libration driven flows may also be of importance in the dynamics and evolution of planetary bodies, notably because of the associated energy dissipation and because of the possibility to generate a magnetic field (see e.g. Le Bars *et al.* 2015, and references therein). However, the details of harmonic flows excited by libration are still largely unknown and controversial (see e.g. Noir *et al.* 2009; Koch *et al.* 2013; Zhang *et al.* 2013; Klein *et al.* 2014).

In a close geometry, an external forcing can resonantly excite global modes (Aldridge & Toomre 1969). In simple geometries, such as the cylinder or the sphere, these modes can be described by so-called inviscid Kelvin modes. Even in these cases, the viscous correction to these modes does exhibit internal shear layers. These layers are associated with corners of the geometry, as in a cylinder (McEwan 1970), or with scaling variations of the viscous boundary layer close to critical latitudes. Kerswell (1995) demonstrated that whether the boundary is concave or convex at the critical latitude, different internal shear layers are expected. From a concave boundary, the boundary layer eruption, which is on a large $O(E^{1/5})$ region, is transmitted throughout the interior without modification (Kida 2011), while it is transmitted and smoothed on a smaller $O(E^{1/3})$ width from a convex boundary (Kerswell 1995). It is this second kind of internal shear layer that will be our interest in the present work. We shall in particular correct the prediction in $O(E^{1/6})$ found in the literature for the amplitude of the solution in this layer (e.g. Kerswell 1995; Calkins *et al.* 2010).

When the geometry is more complex, as in a shell, other types of internal shear layers can be observed. Some of them result from the viscous smoothing of an inviscid attractor (e.g. Rieutord & Valdettaro 1997).

Internal shear layers have been first studied in the context of stationary flows. Many works have concerned disks (Stewartson 1957; Moore & Saffman 1969; van de Vooren 1992) or spheres (Proudman 1956; Stewartson 1966; Marcotte, Dormy & Soward 2016). Similarity solutions have been introduced for their description by Moore & Saffman (1969) for rotating flows and by Thomas & Stevenson (1972) for stratified fluids. Their properties have been reviewed by Voisin (2003). Extensions to more general situations can also be found in Stevenson, Bearon & Thomas (1974) and Peat (1978). These similarity solutions describe the viscous smoothing in a $O(E^{1/3})$ layer of an inviscid singularity propagating along a characteristic line. These solutions

depend on a real parameter which characterizes the strength of the singularity. This parameter also controls the amplitude of the solution and its decay rate from the source (Machicoane *et al.* 2015). Surprisingly, these solutions were also found to be able to describe the fine viscous structure resulting from an attractor (Walton 1975; Rieutord, Georgeot & Valdetaro 2001; Ogilvie 2005).

The paper is organized as follows. In §2, the basic equations and the similarity solutions are introduced. The numerical tool is also described. In §3, we consider the case of a librating disk. We show that the internal shear layers obtained from the numerical simulations are well described by the similarity solutions derived from the asymptotic analysis. In §4, we analyse the case of librating spheroids. We first perform an asymptotic analysis of the viscous boundary layer in the neighbourhood of the critical latitude to compute the characteristics of the similarity solutions. The asymptotic results are then validated using the simulation. In the last section §5, the consequences of the results are briefly discussed.

2. Theoretical background

2.1. Basic equations

We consider the flow generated by the libration of an axisymmetric object in a viscous incompressible rotating fluid. The fluid rotates with an angular rotation Ω^* around the symmetry axis Oz of the object. The frequency and amplitude of the libration are ω^* and ε^* , respectively, such that the angular rotation vector of the object surface can be written as $\boldsymbol{\Omega}_S^*(t) = (\Omega^* + \varepsilon^* \cos(\omega^*t))\mathbf{e}_z$. The frequency is chosen in the inertial wave regime $0 < \omega^* < 2\Omega^*$ such that we can define a propagation angle θ_c satisfying $\omega^* = 2\Omega^* \cos \theta_c$. The angle θ_c defines the direction (with respect to the horizontal plane Oxy) of propagation of the inertial wave of frequency ω^* . It also corresponds to the inclination angle of the internal shear layers.

We shall be interested in the internal shear layers that are generated from disks and spheroids. These internal shear layers are issued from the border of the disk or from the boundary points of the spheroid corresponding to a critical latitude, which is such that the direction normal to the object makes an angle θ_c with respect to the rotation axis Oz .

In the following, time and space variables are non-dimensionalized using $1/\Omega^*$ and the distance r_c^* of the internal shear layer source to the rotation axis, respectively. In non-dimensionalized form, the libration frequency and amplitude are then written as

$$\omega = 2 \cos \theta_c, \quad \varepsilon = \varepsilon^*/\Omega^*. \quad (2.1a,b)$$

The dynamic, which is assumed to remain axisymmetrical, is analysed in a cylindrical rotating frame such that the internal shear layer source is located on a ring at $\mathbf{x}_c = (r_c, z_c) = (1, 0)$. This choice implicitly assumes that the source is not on the rotation axis.

Our objective is to describe the internal shear layer structures of the harmonic response to libration in the limit of small viscosity. Both the libration amplitude ε and the Ekman number

$$E = \frac{\nu}{\Omega^*(r_c^*)^2}, \quad (2.2)$$

where ν is the kinematic viscosity of the fluid, are therefore assumed to be small.

If we write the harmonic response of the velocity and pressure fields as

$$(\mathbf{v}_t, P_t) = \text{Re}\{\varepsilon(\mathbf{v}, p)e^{-i\omega t}\}, \quad (2.3)$$

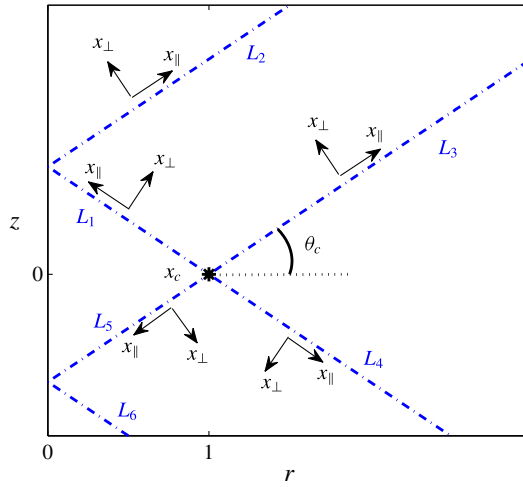


FIGURE 1. (Colour online) Definitions of the lines L_j , $j = 1, 2, 3, 4, 5, 6$ and associated coordinate systems in the (r, z) plane.

its amplitudes \mathbf{v} and p satisfy in the rotating cylindrical frame the equations:

$$-2i \cos \theta_c \mathbf{v} + 2\mathbf{e}_z \wedge \mathbf{v} = -\nabla p + E\nabla^2 \mathbf{v}, \tag{2.4a}$$

$$\nabla \cdot \mathbf{v} = 0. \tag{2.4b}$$

The boundary conditions at infinity and on the object impose

$$\mathbf{v}(\mathbf{x}) = r\mathbf{e}_\phi, \quad \text{on the object surface,} \tag{2.5a}$$

$$\mathbf{v}(\mathbf{x}) \rightarrow 0 \quad \text{as } |\mathbf{x}| \rightarrow \infty. \tag{2.5b}$$

Both \mathbf{v} and p are assumed to depend on r and z only.

2.2. Similarity solution for the description of internal shear layers

As already mentioned above, similarity solutions were introduced by Moore & Saffman (1969) and Thomas & Stevenson (1972). Here, we review some of their properties and introduce our notations. Additional information can be found in Voisin (2003).

By definition, the source point of the similarity solution is $\mathbf{x}_c = (1, 0)$. For a given frequency ω , the propagation occurs along the characteristic lines L_j , $j = 1-6$, as indicated in figure 1. These lines, which actually correspond to sections of cones, make an angle θ_c , defined by (2.1), with respect to the horizontal plane. The four lines L_1, L_3, L_4 and L_5 are the four possible directions of emission from \mathbf{x}_c . The line L_2 (and similarly L_6) is different: it is the continuation of the line L_1 after reflection on the axis of symmetry. Finding the properties of the similarity solution along this line is then slightly more complicated: it requires an analysis of the reflection process on the axis.

We therefore start by the other lines and focus on one of them: L_1 . Along L_1 , we define a local frame $(\mathbf{e}_\parallel, \mathbf{e}_\perp)$ and a local coordinate system (x_\parallel, x_\perp) such that $r\mathbf{e}_r + z\mathbf{e}_z = \mathbf{e}_r + x_\parallel\mathbf{e}_\parallel + x_\perp\mathbf{e}_\perp$ with

$$\mathbf{e}_\parallel = -\mathbf{e}_r \cos \theta_c + \mathbf{e}_z \sin \theta_c, \tag{2.6a}$$

$$\mathbf{e}_\perp = \mathbf{e}_r \sin \theta_c + \mathbf{e}_z \cos \theta_c. \tag{2.6b}$$

In this frame, equations (2.4a,2.4b) can be written as

$$(-2i \cos \theta_c - E\Delta)v_{\parallel} = -2 \cos \theta_c v_{\phi} - \frac{\partial p}{\partial x_{\parallel}}, \tag{2.7a}$$

$$(-2i \cos \theta_c - E\Delta)v_{\perp} = 2 \sin \theta_c v_{\phi} - \frac{\partial p}{\partial x_{\perp}}, \tag{2.7b}$$

$$(-2i \cos \theta_c - E\Delta)v_{\phi} = -2 \sin \theta_c v_{\perp} + 2 \cos \theta_c v_{\parallel}, \tag{2.7c}$$

$$\frac{\partial v_{\perp}}{\partial x_{\perp}} + \frac{\partial v_{\parallel}}{\partial x_{\parallel}} = 2 \cos \theta_c \frac{v_{\parallel}}{r} - 2 \sin \theta_c \frac{v_{\perp}}{r}. \tag{2.7d}$$

Introducing the local transverse scale $\eta_{\perp} = x_{\perp}/E^{1/3}$ and the ansatz

$$v_{\parallel} = \frac{u_{\parallel}^{(0)}}{\sqrt{r}}, \quad v_{\perp} = E^{1/3} \frac{u_{\perp}^{(1)}}{\sqrt{r}}, \quad v_{\phi} = \frac{v_{\phi}^{(0)}}{\sqrt{r}}, \quad p = E^{1/3} \frac{P^{(1)}}{\sqrt{r}} \tag{2.8a-d}$$

we obtain the leading-order equations

$$v_{\phi}^{(0)} = i v_{\parallel}^{(0)}, \tag{2.9a}$$

$$\frac{\partial P^{(1)}}{\partial \eta_{\perp}} = 2i \sin \theta_c v_{\parallel}^{(0)}, \tag{2.9b}$$

$$\frac{\partial v_{\perp}^{(1)}}{\partial \eta_{\perp}} = -\frac{\partial v_{\parallel}^{(0)}}{\partial x_{\perp}} - \cos \theta_c \frac{v_{\parallel}^{(0)}}{2r}, \tag{2.9c}$$

$$i \frac{\partial^3 v_{\parallel}^{(0)}}{\partial \eta_{\perp}^3} + 2 \sin \theta_c \frac{\partial v_{\parallel}^{(0)}}{\partial x_{\parallel}} = 0. \tag{2.9d}$$

Similarity solutions are obtained by searching $v_{\parallel}^{(0)}$ in the form

$$v_{\parallel}^{(0)} = C_0 H_m(x_{\parallel}, \zeta) = C_0 \left(\frac{x_{\parallel}}{2 \sin \theta_c} \right)^{-m/3} h_m(\zeta), \tag{2.10}$$

where m is a real number, C_0 a complex constant and

$$\zeta = \eta_{\perp} \left(\frac{2 \sin \theta_c}{x_{\parallel}} \right)^{1/3}. \tag{2.11}$$

The function h_m is found to satisfy

$$3h_m''' + i\zeta h_m' + imh_m = 0. \tag{2.12}$$

As shown by Moore & Saffman (1969), the solution which is bounded for $m > 0$ is a multiple of

$$h_m(\zeta) = \frac{e^{-im\pi/2}}{(m-1)!} \int_0^{+\infty} e^{ip\zeta - p^3} p^{m-1} dp. \tag{2.13}$$

The normalization of h_m has been chosen such that

$$H_m(x_{\parallel}, \zeta) \underset{\zeta \rightarrow +\infty}{\sim} \eta_{\perp}^{-m}, \tag{2.14a}$$

$$H_m(x_{\parallel}, \zeta) \underset{\zeta \rightarrow -\infty}{\sim} (-\eta_{\perp})^{-m} e^{-im\pi}. \tag{2.14b}$$

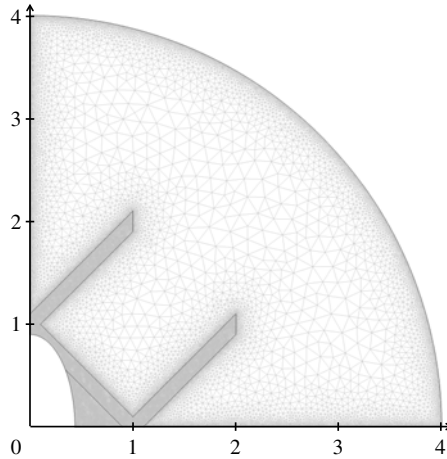


FIGURE 2. Geometry and grid of the numerical simulation, shown here for a prolate spheroid of eccentricity $\sqrt{2/3}$.

The other components can be deduced from (2.9a–c). Here we shall only use the expression for the azimuthal velocity:

$$v_{\phi}^{(0)} = iC_0 H_m(x_{\parallel}, \zeta). \quad (2.15)$$

The above analysis applies to L_1 . A similar analysis can be performed on the other lines L_3 , L_4 and L_5 . With the definition of the coordinate system shown in figure 1, we obtain the same expression (2.10) for $v_{\parallel}^{(0)}$ with ζ defined by (2.11) for all these lines. However, (2.15) is valid on the lines L_1 and L_5 only. On the symmetric lines L_3 and L_4 , we must use

$$v_{\phi}^{(0)} = -iC_0 H_m(x_{\parallel}, \zeta). \quad (2.16)$$

As shown in appendix A, on L_2 , we should use the formula

$$v_{\parallel}^{(0)} = iC_0 H_m(x_{\parallel}, \zeta), \quad v_{\phi}^{(0)} = C_0 H_m(x_{\parallel}, \zeta), \quad (2.17a,b)$$

with $x_{\parallel} = (r + 1) \cos \theta_c + z \sin \theta_c$ (that is counted from a symmetric source at $(-1, 0)$).

2.3. Description of the numerical method

Axisymmetric direct numerical simulations are performed with the finite-element commercial software Comsol Multiphysics. Incompressible Navier–Stokes equations are solved for a Newtonian fluid in the frame of reference rotating at the mean angular velocity Ω^* . The length scale in the numerics is the axis distance to the point where the characteristic line L_4 crosses the equator. Considering the axial and equatorial symmetries of the problem, the fluid domain then corresponds to the upper right quarter of a sphere of radius 4 (see figure 2). Boundary conditions are stress free at the spherical radial coordinate $\rho = 4$, no slip with imposed libration azimuthal velocity $\mathbf{v} = \varepsilon r \cos(\omega t) \mathbf{e}_{\phi}$ at the object boundary and symmetry conditions along the rotation axis. Regarding the librating disk problem, we consider 2 configurations for the boundary conditions along the equatorial plane: either $\mathbf{v} = \mathbf{0}$, which we refer to as the ‘disk in a solid plane’ configuration, or symmetry conditions (that is

$v_z = \partial_z v_r = \partial_z v_\phi = 0$ at $z = 0$ outside the object), which we refer to as the ‘free disk’ configuration. Symmetry conditions are also used for all the spheroidal geometries. From $\rho = 2$ to $\rho = 4$, the viscosity increases exponentially with the radius squared by a factor of approximately 2000, so as to damp outgoing propagating waves: any wave reflected from the outer boundary is then negligible. The mesh is made of triangular standard Lagrange elements of type P3–P2 (i.e. cubic for the velocity field and quadratic for the pressure field). It is strongly refined close to the boundaries and along the characteristic lines, where rapid variations of the velocity field are expected (see figure 2). The total number of degrees of freedom ranges between 800 000 and 1.2 million, depending on the geometry of the librating object. At each time step, the system is solved with the sparse direct linear solver PARDISO and the backward difference formulae temporal solver with a maximal order 2. The time step is limited to 1/150 of the libration period. No stabilization technique is used. Starting from $\mathbf{v} = \mathbf{0}$ everywhere in the fluid at time $t = t_i = -\pi/(2\omega)$, the computation is first run during 250 libration cycles so as to reach a steady state; the 5 next oscillations are then recorded and analysed. We have checked that our results are not significantly affected by changing the grid, the size of the domain, the coefficient of the viscous exponential increase or the maximum time step.

3. Libration of a disk

3.1. Summary of the asymptotic results for the disk in a solid plane

Le Dizès (2015) provided an asymptotic expression of the solution for the librating disk in a solid plane in the limit of small Ekman numbers. In the inertial wave regime ($0 < \omega < 2$), he found, using results by Tilgner (2000) that, outside the boundary layer on the disk ($z \gg \sqrt{E}$), the velocity amplitude of the harmonic solution can be written with the present notation as

$$\mathbf{u} = A(2\mathbf{u}_D - \mathbf{u}_R), \tag{3.1}$$

with

$$A = \frac{\sqrt{E}}{2 \sin \theta_c} e^{i(\pi/4) - i(\theta_c/2)}, \tag{3.2}$$

where the two contributions \mathbf{u}_D and \mathbf{u}_R correspond to the solutions generated from a uniform axial oscillating forcing on the disk of unitary amplitude and from a Dirac oscillating ring source of axial flow on the disk edge, respectively. These contributions are given by

$$\mathbf{u}_D = \begin{cases} u_D = -i \frac{\cos \theta_c}{\sin \theta_c} I_D^{(1)} \\ v_D = -\frac{1}{\sin \theta_c} I_D^{(1)} \\ w_D = I_D^{(0)} \end{cases} \quad \text{and} \quad \mathbf{u}_R = \begin{cases} u_R = -i \frac{\cos \theta_c}{\sin \theta_c} I_R^{(1)} \\ v_R = -\frac{1}{\sin \theta_c} I_R^{(1)} \\ w_R = I_R^{(0)}, \end{cases} \tag{3.3a,b}$$

with

$$I_D^{(m)} = \int_0^\infty J_1(k) J_m(kr) e^{ikz} e^{-\tilde{E}k^3 z} dk, \tag{3.4a}$$

$$I_R^{(m)} = \int_0^\infty k J_0(k) J_m(kr) e^{ikz} e^{-\tilde{E}k^3 z} dk, \tag{3.4b}$$

where

$$\tilde{z} = \frac{\cos \theta_c}{\sin \theta_c} z, \quad \tilde{E} = \frac{E}{2 \cos \theta_c \sin^4 \theta_c}. \tag{3.5a,b}$$

Without the diffusing factor $e^{-\tilde{E}k^3\tilde{z}}$ the integrals $I_D^{(m)}$ and $I_R^{(m)}$ are singular on the characteristic lines L_j shown in figure 1. These lines correspond to the conical structure along which the singularity at the edge of the disk propagates. Close to these lines, the functions $I_D^{(m)}$ and $I_R^{(m)}$ take a particular form as E goes to zero. The function $I_D^{(m)}$ is $O(-\log(E))$ while $I_R^{(m)}$ becomes $O(E^{-1/3})$. The part associated with the ring source therefore provides the dominant contribution to the solution. Close to each line, the velocity field is found to be mainly aligned along with the conical structure. The two velocity components v_{\parallel} and v_{ϕ} (aligned along with L_j and the azimuthal direction, respectively) are found to be identical albeit a phase factor. Around the line L_1 , Le Dizès (2015) showed that the solution can be written as (2.8) with

$$v_{\parallel}^{(0)} = -\frac{\sqrt{E}}{4 \sin \theta_c} e^{i(\pi/4) - i(\theta_c/2)} \left(\frac{2 \sin^2 \theta_c}{3Ez}\right)^{1/3} \mathbf{Hi} \left(ix_{\perp} \left(\frac{2 \sin^2 \theta_c}{3Ez}\right)^{1/3} \right). \tag{3.6}$$

If we recall that the Scorer function \mathbf{Hi} can be expressed in terms of h_1 as

$$\mathbf{Hi}(s) = \frac{3^{1/3}i}{\pi} h_1(-i3^{1/3}s) \tag{3.7}$$

and that $z \sim \sin \theta_c x_{\parallel}$ close to L_1 , expression (3.6) is found to be of the form (2.10) with

$$m = 1, \tag{3.8a}$$

$$C_0 = \frac{E^{1/6}}{4\pi \sin \theta_c} e^{-i(\pi/4) - i(\theta_c/2)}. \tag{3.8b}$$

The same expressions are obtained for the other lines L_j , $j = 2, 3, 4, 5, 6$.

3.2. Numerical results

In this section, we provide numerical results for both the disk in a solid plane and the disk in a free space. The numerical solution is analysed after 250 periods such that transience has disappeared and a periodic regime has been reached. For the value $\varepsilon = 10^{-4}$ that we consider, the solution is dominated by the harmonic response. A small Ekman number $E = 10^{-5}$ is also chosen such that the solutions can be compared to the asymptotic expressions given in the previous section. We have chosen a fixed normalized frequency $\omega = \sqrt{2}$ such that $\theta_c = \pi/4$.

In figure 3, a typical contour plot of the azimuthal velocity is shown in the (r, z) plane at a given time for the case of the free disk. In figure 4, the velocity components of the numerical solutions obtained for a free disk and for a disk in a solid plane are plotted as a function of z in the vertical sections C_1 and C_2 corresponding to $r = 1/2$ and $r = 3/2$ respectively. The asymptotic solution (3.1) is also plotted in these graphs at the same instant. We can see that the free disk and the disk in a solid plane solutions are very close to each other and well described by the asymptotic solution.

The similarity structure of the numerical solutions is also analysed in figure 5. In this figure, we plot v_{ϕ} and v_{\parallel} , normalized by the amplitude factor $A = \varepsilon|C_0|$

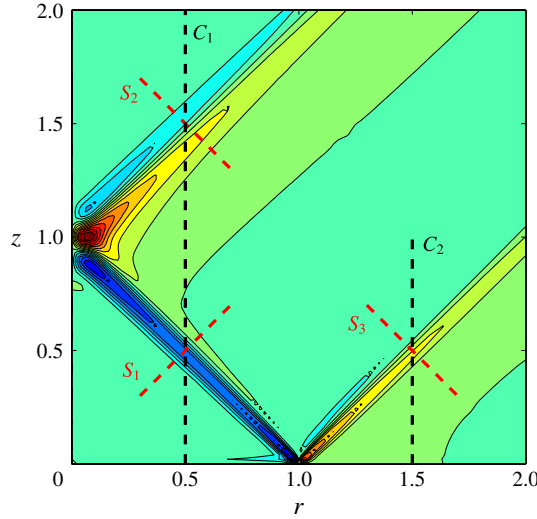


FIGURE 3. (Colour online) Contour of the azimuthal velocity v_ϕ in the (r, z) plane of the librating disk for a disk in a solid plane configuration obtained from the numerical simulation at $t = 501.5\pi/\omega$ for $E = 10^{-5}$, $\varepsilon = 10^{-4}$, $\omega = \sqrt{2}$. The sections C_k , $k = 1, 2$ and S_j , $j = 1, 2, 3$ where the profiles are analysed in figures 4 and 5 are also indicated.

$(2 \sin \theta_c/x_\parallel)^{1/3}/\sqrt{r}$ with respect to the similarity variable ζ defined in (2.11) with the expression (3.8b) for C_0 . We consider the numerical solutions in the sections S_1 , S_2 and S_3 indicated in figure 3 at the same time. These solutions are compared to the theoretical predictions, which can be written after the renormalization as

$$V_\parallel^{SS} = \text{Re}(h_1(\zeta)e^{-i\varphi_\parallel}), \quad V_\phi^{SS} = \text{Im}(h_1(\zeta)e^{-i\varphi_\phi}), \quad (3.9a,b)$$

where

$$\varphi_\parallel = \varphi_\phi = \omega t_o + 3\pi/8 \quad \text{for } S_1, \quad (3.10a)$$

$$\varphi_\parallel = \varphi_\phi + \pi = \omega t_o - \pi/8 \quad \text{for } S_2, \quad (3.10b)$$

$$\varphi_\parallel = \varphi_\phi + \pi = \omega t_o + 3\pi/8 \quad \text{for } S_3. \quad (3.10c)$$

In figure 6, the solutions are analysed along the lines L_j . We plot the norm of the velocity vector, normalized by $1/(x_\parallel^{1/3}\sqrt{r})$, along the lines L_j (that is for $x_\perp = 0$) as a function of x_\parallel for different times. The theory predicts that this factor should be constant for all times and equal to

$$|\mathbf{v}|x_\parallel^{1/3}\sqrt{r} \sim \varepsilon|h_1(0)| |C_0|(2 \sin \theta_c)^{1/3} \approx 0.0895 \frac{\varepsilon E^{1/6}}{(\sin \theta_c)^{2/3}}. \quad (3.11)$$

This prediction has been indicated as a red dashed line in figure 6. We do observe that the numerical results follow relatively well the theoretical prediction. The departure between L_1 and L_2 corresponds to the region close to the rotation axis where the theory is known to be not applicable. We observe that the numerics provide systematically smaller values than the theory, especially on the line L_3 . In the future, it would be interesting to consider smaller Ekman numbers in the numerics to check that this discrepancy is indeed associated with the not sufficiently small value of the Ekman number.

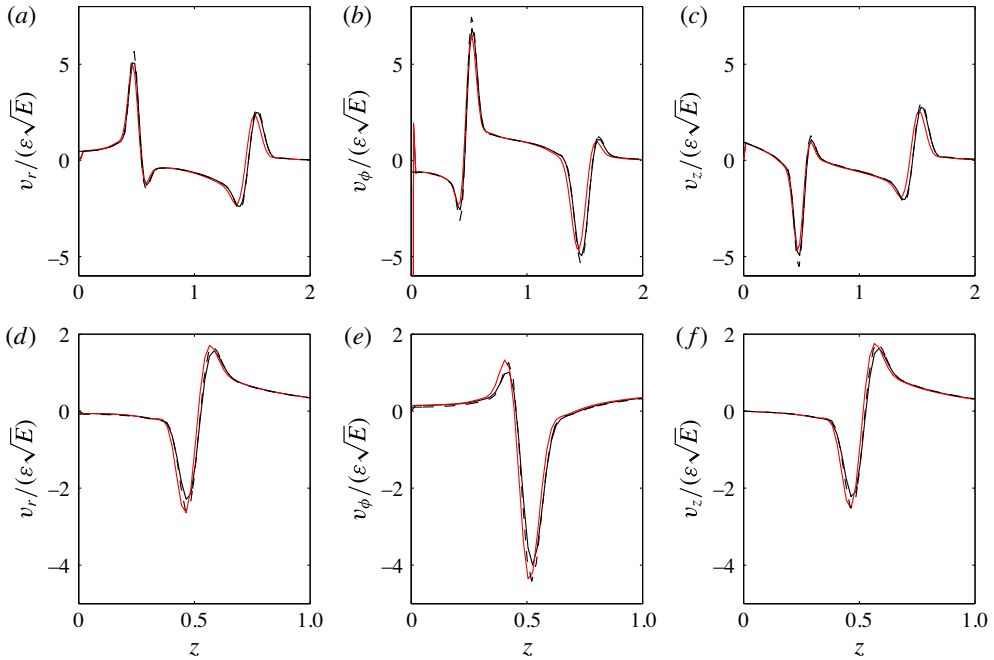


FIGURE 4. (Colour online) Velocity profiles ((a,d) v_r , (b,e) v_ϕ , (c,f) v_z) normalized by $\varepsilon\sqrt{E}$ along the vertical cut at $r=0.5$ (a–c) and at $r=1.5$ (d–f) for $E=10^{-5}$, $\varepsilon=10^{-4}$, $\omega=\sqrt{2}$ at $t_o=508.9\pi/\omega$. Solid lines are numerical results (in black the disk, in a solid plane, in red the free disk) while dashed lines are asymptotic results for the disk in a solid plane.

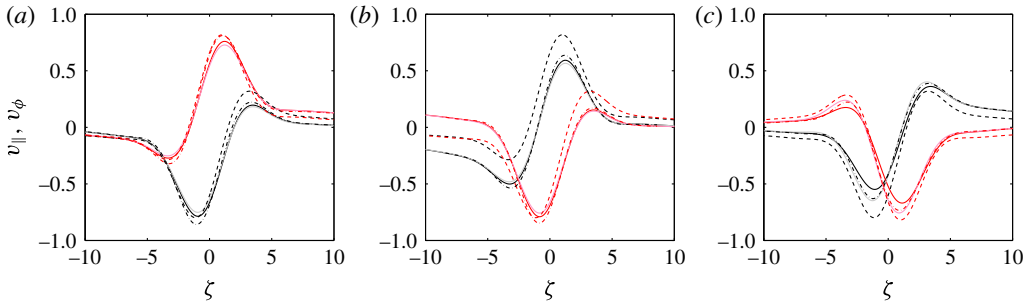


FIGURE 5. (Colour online) Velocity profiles across the internal shear layer in the sections S_1 (a), S_2 (b) and S_3 (c) (see figure 3) at time $t_o=508.9\pi/\omega$ for $E=10^{-5}$, $\varepsilon=10^{-4}$, $\omega=\sqrt{2}$. Red (v_ϕ) and black (v_\parallel) curves are for the disk in a solid plane, pink (v_ϕ) and grey (v_\parallel) are for the free disk. Solid lines are numerical results. The other lines are asymptotic results. Dash-dotted lines: asymptotic formula (3.1) with ring and disk contributions. Dashed lines: similarity solution constructed using (3.8a,b). All the solutions have been renormalized by the factor $A=\varepsilon|C_0|(2\sin\theta_c/x_\parallel)^{1/3}/\sqrt{r}$ with C_0 given by (3.8b).

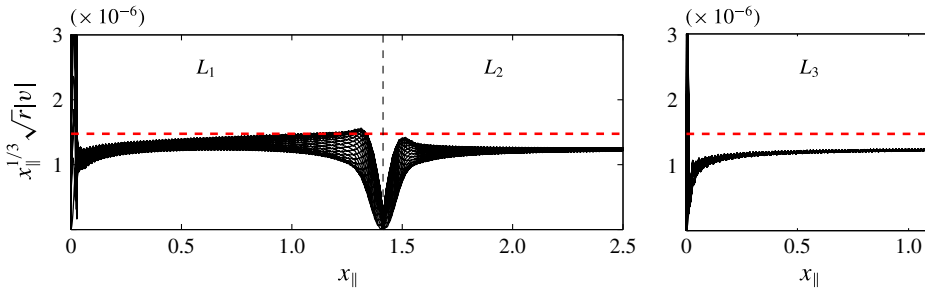


FIGURE 6. (Colour online) Norm of the velocity vector along the characteristic lines L_j normalized by $r^{-1/2}x_{\parallel}^{-1/3}$ for a libration disk in a solid plane. $E = 10^{-5}$, $\varepsilon = 10^{-4}$, $\omega = \sqrt{2}$, $\theta_c = \pi/4$. The solid black lines are the numerical results obtained for time $\omega t/(2\pi) = 250 : 1/25 : 251$. The dashed line is expression (3.11).

4. Libration of a spheroid

In this section, we analyse the flow generated by the libration of a spheroid. We have no asymptotic solution for this geometry but we suspect that the flow structure around the characteristic rays tangent to the spheroid corresponds to one of the similarity solutions described in §2.2. To obtain the parameter m and the amplitude factor C_0 of the solution, we perform an asymptotic analysis close to the critical latitude x_c . More precisely, these parameters are obtained by the condition of matching close to x_c of the boundary layer solution on the object with the similarity solution. The theoretical result is then tested and validated using direct numerical simulations.

4.1. Asymptotic analysis close to x_c

4.1.1. Boundary layer solution

In this section, we consider an arbitrary axisymmetric convex object librating and rotating around its axis of symmetry Oz . We analyse the solution in a plane Σ containing this axis Oz . In this plane, we assume that the object surface is described by a smooth curve $(r(s), z(s))$, with tangential and normal vectors defined by

$$\mathbf{t} = \frac{r'\mathbf{e}_r + z'\mathbf{e}_z}{\alpha}, \quad \mathbf{n} = \frac{-z'\mathbf{e}_r + r'\mathbf{e}_z}{\alpha}, \tag{4.1a,b}$$

with

$$\alpha = \sqrt{r'^2 + z'^2}, \tag{4.2}$$

where the prime denotes derivative with respect to s . The surface being convex, any point $M(\xi, \chi)$ in the fluid (outside the object) is identified by a curvilinear abscissa s and a distance x_n to the surface such that $OM = \xi\mathbf{e}_r + \chi\mathbf{e}_z = r(s)\mathbf{e}_r + z(s)\mathbf{e}_z + x_n\mathbf{n}$ (see figure 7a). We assume that the critical latitude x_c on the surface is reached at $s = s_c$. At such a point, the tangential and normal vectors are given by

$$\mathbf{t}_c = \cos\theta_c\mathbf{e}_r - \sin\theta_c\mathbf{e}_z, \quad \mathbf{n}_c = \sin\theta_c\mathbf{e}_r + \cos\theta_c\mathbf{e}_z. \tag{4.3a,b}$$

We therefore have the following equalities:

$$r(s_c) = r_c = 1, \quad z(s_c) = z_c = 0, \tag{4.4a,b}$$

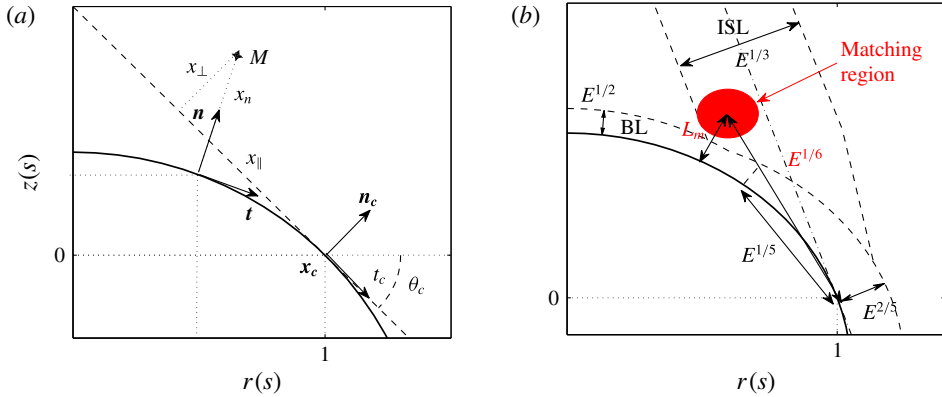


FIGURE 7. (Colour online) (a) Definition of the coordinate systems near x_c . (b) Sketch of the different regions of the asymptotic analysis. The region of matching is at $O(E^{1/6})$ from x_c within the internal shear layer (ISL) but outside the boundary layer (BL), i.e. at a distance L_m from the boundary satisfying $E^{5/12} \ll L_m \ll E^{1/3}$.

$$r'(s_c) = r'_c = \alpha_c \cos \theta_c, \quad z'(s_c) = z'_c = -\alpha_c \sin \theta_c. \tag{4.4c,d}$$

Introducing the boundary layer variable $\eta = x_n/\sqrt{E}$ and the following ansatz for the pressure and velocity components along t , n and e_ϕ :

$$p = \sqrt{E} \bar{p}^{(1)}(s, \eta), \quad v_t = \bar{v}_t^{(0)}(s, \eta), \quad v_n = \sqrt{E} \bar{v}_n^{(1)}(s, \eta), \quad v_\phi = \bar{v}_\phi^{(0)}(s, \eta), \tag{4.5a-d}$$

we get from (2.4a,b)

$$\left(-2i \cos \theta_c - \frac{\partial^2}{\partial \eta^2}\right) \bar{v}_t^{(0)} - 2 \frac{r'}{\alpha} \bar{v}_\phi^{(0)} = 0, \tag{4.6a}$$

$$\left(-2i \cos \theta_c - \frac{\partial^2}{\partial \eta^2}\right) \bar{v}_\phi^{(0)} + 2 \frac{r'}{\alpha} \bar{v}_t^{(0)} = 0, \tag{4.6b}$$

$$2 \frac{z'}{\alpha} \bar{v}_\phi^{(0)} = \frac{\partial \bar{p}^{(1)}}{\partial \eta}, \tag{4.6c}$$

$$\frac{\partial \bar{v}_n^{(1)}}{\partial \eta} + \frac{1}{\alpha} \frac{\partial \bar{v}_t^{(0)}}{\partial s} + \frac{r'}{r\alpha} \bar{v}_t^{(0)} = 0. \tag{4.6d}$$

With the boundary conditions (2.5), the two first equations immediately give

$$\bar{v}_\phi^{(0)} = \frac{r(s)}{2} (e^{-\lambda_-\eta} + e^{-\lambda_+\eta}), \tag{4.7a}$$

$$\bar{v}_t^{(0)} = \frac{ir(s)}{2} (e^{-\lambda_-\eta} - e^{-\lambda_+\eta}), \tag{4.7b}$$

where the functions

$$\lambda_\pm = \sqrt{-2i \left(\cos \theta_c \pm \frac{r'}{\alpha} \right)} \tag{4.8}$$

are such that $\text{Re}(\lambda_{\pm}) > 0$. The third equation (4.6c) can be used to get the pressure field, while (4.6d) gives

$$\begin{aligned} \bar{v}_n^{(1)} = & \frac{ir(s)\eta}{2\alpha} \left(\frac{\lambda'_+}{\lambda_+} e^{-\lambda_+\eta} - \frac{\lambda'_-}{\lambda_-} e^{-\lambda_-\eta} \right) + \left(\frac{ir'}{2\alpha\lambda_-} - \frac{ir\lambda'_-}{2\alpha\lambda_-^2} \right) (e^{-\lambda_-\eta} - 1) \\ & - \left(\frac{ir'}{2\alpha\lambda_+} - \frac{ir\lambda'_+}{2\alpha\lambda_+^2} \right) (e^{-\lambda_+\eta} - 1). \end{aligned} \tag{4.9}$$

This last expression can be used to obtain the Ekman pumping in the bulk. We are especially interested in its expression close to \mathbf{x}_c when s goes to s_c . Here we consider the situation illustrated in figure 7(b), which corresponds to L_1 . For this case, s is always smaller than s_c . Close to s_c , λ_+ remains finite but λ_- goes to zero as

$$\lambda_- \sim (1+i)\sqrt{-\kappa_c\alpha_c \sin\theta_c(s_c-s)}, \tag{4.10}$$

where κ_c is the local curvature at \mathbf{x}_c . The curvature κ is defined by

$$\kappa = \frac{z''r' - r''z'}{\alpha^3}. \tag{4.11}$$

Here, it is negative in the neighbourhood of \mathbf{x}_c .

If we perform the limits $\eta \rightarrow \infty$ (first) and $s \rightarrow s_c$ (second), we get a normal velocity which behaves as

$$v_n \sim \frac{(1+i)}{8\alpha_c^{3/2}\sqrt{-\kappa_c \sin\theta_c}} \frac{\sqrt{E}}{(s_c-s)^{3/2}}. \tag{4.12}$$

This limit is valid as long as $\eta\sqrt{s_c-s} \rightarrow \infty$ when $s \rightarrow s_c$.

4.1.2. Similarity solution near \mathbf{x}_c

The similarity solutions introduced in §2.2 are singular as we get close to \mathbf{x}_c . For a fixed η_{\perp} , this amounts to considering the limit $x_{\parallel} \rightarrow 0$. As we are interested in the solution close to the boundary for L_1 , we consider a negative η_{\perp} (see figure 7b) such that ζ defined by (2.11) goes to $-\infty$ as $x_{\parallel} \rightarrow 0$. In this limit, we obtain

$$v_{\parallel} \sim C_0(-\eta_{\perp})^{-m} e^{-im\pi}, \tag{4.13a}$$

$$v_{\perp} \sim -C_0 E^{1/3} \frac{\cos\theta_c}{2(m-1)} (-\eta_{\perp})^{-m+1} e^{-im\pi}. \tag{4.13b}$$

These estimates apply as long as $-\eta_{\perp}(x_{\parallel})^{-1/3} \gg 1$.

4.1.3. Matching

In this section, we show that the similarity solution and the boundary layer solution are compatible for particular values of C_0 and m . The matching is performed in the region where both expressions (4.12) and (4.13) apply. To determine this region, it is useful to express the variables x_{\parallel} and η_{\perp} in terms of the boundary layer variables s and η :

$$x_{\parallel} = -\cos\theta_c \left(r(s) - 1 - \sqrt{E}\eta \frac{z'}{\alpha} \right) + \sin\theta_c \left(z(s) + \sqrt{E}\eta \frac{r'}{\alpha} \right), \tag{4.14a}$$

$$\eta_{\perp} = \frac{\sin\theta_c}{E^{1/3}} \left(r(s) - 1 - \sqrt{E}\eta \frac{z'}{\alpha} \right) + \frac{\cos\theta_c}{E^{1/3}} \left(z(s) + \sqrt{E}\eta \frac{r'}{\alpha} \right). \tag{4.14b}$$

Close to \mathbf{x}_c , these expressions become

$$x_{\parallel} \sim \alpha_c(s_c - s) + \sqrt{E}\kappa_c\alpha_c\eta(s_c - s), \tag{4.15a}$$

$$\eta_{\perp} \sim E^{1/6}\eta + E^{-1/3}\kappa_c\alpha_c^2\frac{(s_c - s)^2}{2}, \tag{4.15b}$$

where we recall that κ_c is the curvature at \mathbf{x}_c .

If $|s - s_c| = O(E^{1/6})$ and $E^{-1/12} \ll \eta \ll E^{-1/6}$, we do have $\sqrt{|s - s_c|}\eta \gg 1$ as required by (4.12). Moreover, we then obtain

$$x_{\parallel} \sim \alpha_c(s_c - s), \tag{4.16a}$$

$$\eta_{\perp} \sim E^{-1/3}\kappa_c\alpha_c^2\frac{(s - s_c)^2}{2}, \tag{4.16b}$$

which implies that $-\eta_{\perp}x_{\parallel}^{-1/3} \propto E^{-1/3}(s_c - s)^{5/3} = O(E^{-1/18}) \gg 1$ as required for the validity of (4.13). This region is materialized in red in the sketch shown in figure 7(b). In this figure, we have also indicated the scalings of the different asymptotic regions: the $O(E^{1/2})$ width of the boundary layer on the object far from s_c , the $O(E^{1/3})$ width of the similarity solution around L_1 far from s_c , and the scalings in $E^{1/5}$ and $E^{2/5}$ of the local region near s_c where the singularities of both the boundary layer solution and the similarity solution are smoothed (Roberts & Stewartson 1963; Kerswell 1995).

In this region, we can then match the boundary layer solution with the similarity solution. The normal velocity v_n can be deduced from v_{\parallel} and v_{\perp} using

$$v_n = \frac{1}{\alpha}((z' \cos \theta_c + r' \sin \theta_c)v_{\parallel} + (-z' \sin \theta_c + r' \cos \theta_c)v_{\perp}), \tag{4.17}$$

which becomes close to s_c

$$v_n \sim v_{\perp} - \kappa_c\alpha_c(s_c - s)v_{\parallel}. \tag{4.18}$$

If we take into account (4.16a,b), the normal velocity obtained from the similarity solution (4.13a,b) is therefore

$$v_n \sim E^{m/3}(-\kappa_c)^{-m+1}2^m\alpha_c^{-2m+1}(s_c - s)^{-2m+1}C_0e^{-im\pi}. \tag{4.19}$$

This expression is compatible with (4.12) if and only if

$$m = 5/4, \tag{4.20a}$$

$$C_0 = \frac{E^{1/12}}{8\sqrt{2} \sin \theta_c (-2\kappa_c)^{1/4}} e^{-i\pi/2}. \tag{4.20b}$$

These expressions for m and C_0 apply for the similarity solution along the line L_1 . A similar analysis can be carried out for the similarity solution along L_4 by performing the matching on the other side of \mathbf{x}_c . It gives the same value of m and an amplitude C_0 just differing by a phase factor:

$$C_0 = \frac{E^{1/12}}{8\sqrt{2} \sin \theta_c (-2\kappa_c)^{1/4}} e^{-i\pi/4}. \tag{4.21}$$

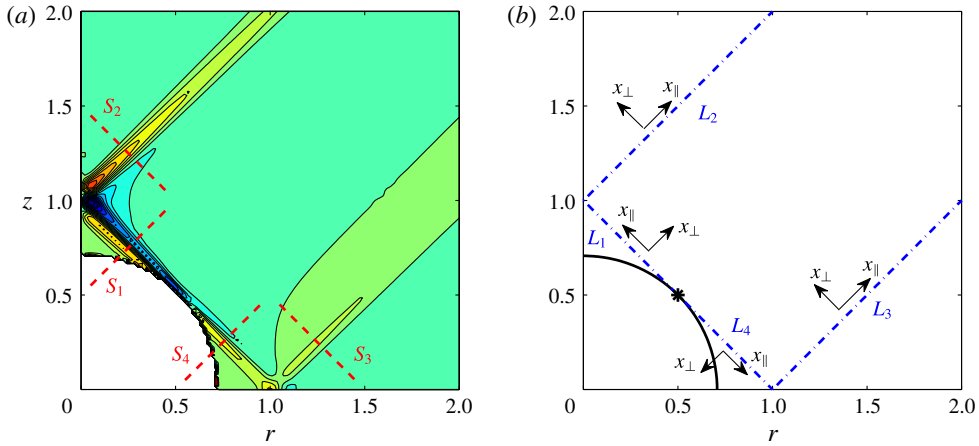


FIGURE 8. (Colour online) (a) Contour of the azimuthal velocity v_ϕ in the (r, z) plane of a librating sphere obtained from the numerical simulation at time $t = 508.9\pi/\omega$ for $E_s = 10^{-5}$, $\varepsilon = 10^{-4}$, $\omega = \sqrt{2}$. The sections S_j , $j = 1, 2, 3, 4$, where the profiles are analysed in figure 9, are also indicated. (b) Definition of the local coordinate system on the characteristic lines L_j , $j = 1, 2, 3, 4$. The star indicates the source point of the similarity solutions.

These values of m and C_0 constitute the main result of the present paper. In particular, it is worth mentioning that the value of m is larger for a smooth surface (spheroid) than for an angular one (disk). This means that we have the following counter-intuitive result: the similarity solution describing the internal shear layer is associated with a stronger singularity at \mathbf{x}_c for a smooth surface than for an angular one. As a consequence, the amplitude of the velocity field is larger for the spheroid with a scaling in $E^{1/12}$ to be compared with the $E^{1/6}$ scaling for the disk. Expressions (4.20b) and (4.21) provide the dependency with respect to the libration frequency through the term $2 \sin \theta_c = \sqrt{4 - \omega^2}$. The amplitude of the internal shear layer increases when θ_c decreases, that is when ω gets close to 2 (or ω^* close to $2\Omega^*$). We can also note the dependency with respect to the local curvature κ_c . The amplitude decreases as $|\kappa_c|$ increases. The more peaky the surface at \mathbf{x}_c is, the smaller the amplitude of the internal shear layer is. This is consistent with the smaller amplitude scaling obtained for the singular case of the disk.

4.2. Comparison with numerical results

In this section, the formulas (4.20a,b) are tested against direct numerical simulations. Different spheroids as well as different frequencies are considered.

The numerical simulations were first performed for a sphere of radius $1/\sqrt{2}$ with a frequency $\omega = \sqrt{2}$ such that the singular rays start from the point $\mathbf{x}_c = (1/2, 1/2)$ on the surface and cross the meridional plane and the rotation axis at $(1, 0)$ and $(0, 1)$ respectively, as illustrated in figure 8(a). This normalization does not correspond to that chosen for the similarity solution. The Ekman number of the simulation E_s is therefore 4 times smaller than the Ekman number defined in (2.2). The internal shear layers are emitted on either side of \mathbf{x}_c along the lines L_1 and L_4 indicated in figure 8(b). The internal shear layer on L_1 is reflected on the axis and continues

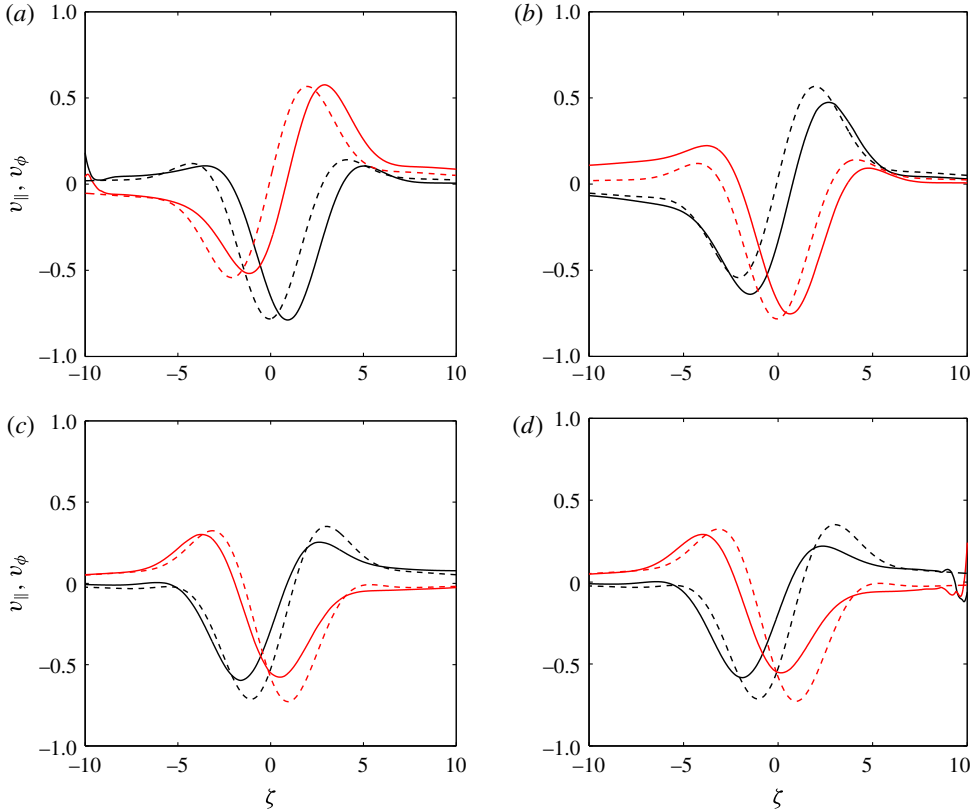


FIGURE 9. (Colour online) Profiles of v_ϕ (red curves) and v_\parallel (black curves) across the internal shear layer in the sections S_1 (a), S_2 (b), S_3 (c) and S_4 (d) as indicated in figure 8, at time $t = 508.9\pi/\omega$ for $E_s = 2.5 \times 10^{-6}$ (i.e. $E = 10^{-5}$), $\varepsilon = 10^{-4}$, $\omega = \sqrt{2}$. Solid lines are numerical results. Dashed lines are the similarity solutions. All the solutions have been renormalized by the factor $A = \varepsilon|C_0|(2 \sin \theta_c/x_\parallel)^{5/4}/\sqrt{r}$ with C_0 given by (4.20b) or (4.21).

along L_2 . The internal shear layer on L_3 corresponds to that emitted from the symmetric point $(1/2, -1/2)$ on the sphere. The definition of the coordinate systems is given in figure 8(b), in agreement with the definition used in figure 1.

In figure 9, we compare the numerical solution to the similarity solution in the sections indicated in figure 8(a) at a particular instant. Both the azimuthal velocity and the parallel velocity are plotted as a function of the similarity variable. As for the disk, the normalization has been chosen such that the theoretical predications for v_ϕ and v_\parallel are just given by

$$V_\parallel^{SS} = \text{Re}(h_{5/4}(\zeta)e^{-i\varphi_\parallel}), \quad V_\phi^{SS} = \text{Im}(h_{5/4}(\zeta)e^{-i\varphi_\phi}), \tag{4.22a,b}$$

where

$$\varphi_\parallel = \varphi_\phi = \omega t_o + \pi/2 \quad \text{for } S_1, \tag{4.23a}$$

$$\varphi_\parallel = \varphi_\phi + \pi = \omega t_o \quad \text{for } S_2, \tag{4.23b}$$

$$\varphi_\parallel = \varphi_\phi + \pi = \omega t_o + \pi/4 \quad \text{for } S_3 \text{ and } S_4. \tag{4.23c}$$

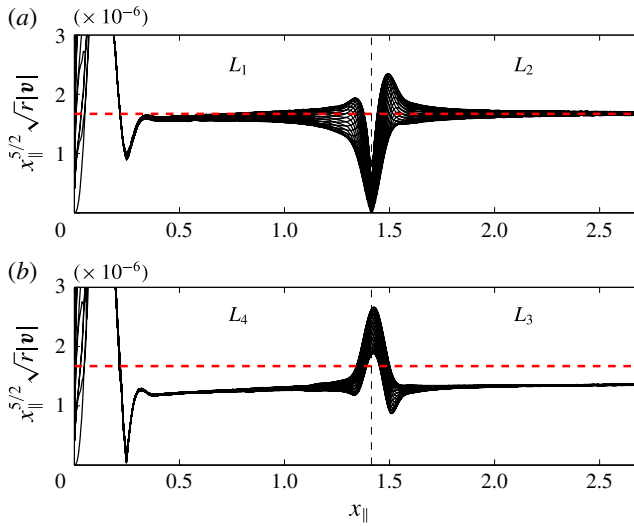


FIGURE 10. (Colour online) Norm of the velocity vector along the characteristic lines L_j normalized by $x_{\parallel}^{-5/2} r^{-1/2}$ for a librating sphere with $E_s = 2.5 \times 10^{-6}$ (i.e. $E = 10^{-5}$), $\varepsilon = 10^{-4}$, $\omega = \sqrt{2}$, $\theta_c = \pi/4$. The solid black lines are the numerical results obtained for time $\omega t/(2\pi) = 250 : 1/25 : 251$. The dashed red line is the theoretical prediction (4.24).

As for the disk, we have also looked at the solution along the characteristic lines L_j . For the spheroid, we expect $|x_{\parallel}|^{5/12} \sqrt{r} |\mathbf{v}|$ to remain constant and uniform and given by

$$|x_{\parallel}|^{5/12} \sqrt{r} |\mathbf{v}| \sim \varepsilon |h_{5/4}(0)| |C_0| (2 \sin \theta_c)^{5/12} \approx 0.0776 \frac{\varepsilon E^{1/12}}{(\sin \theta_c)^{1/12} |\kappa_c|^{1/4}}. \quad (4.24)$$

This is verified in figure 10 where we have plotted $|x_{\parallel}|^{5/12} \sqrt{r} |\mathbf{v}|$ versus x_{\parallel} along the lines L_1 and L_2 (a) and L_4 and L_3 (b) for 25 equidistant times within a period. The theoretical prediction (4.24) is indicated as a red dashed line. The agreement is good for the upper lines L_1 and L_2 . However, as for the disk, there is a weak discrepancy between the theory and the numerics for the constant on the lower lines L_4 and L_3 . Close to $x_{\parallel} \approx \sqrt{2}$, the departures are associated with the impact of L_1 and L_2 on the axis, and with the crossing of L_4 and L_3 .

Other geometries have been tested numerically. We present here two other configurations, a sphere with a different frequency and an oblate spheroid (see figure 11). For both cases, we have performed the same tests. In figure 12, we provide plots of v_{ϕ} and v_{\parallel} in different sections indicated in figure 11 using the same normalization as above such that formulas (4.22) still apply. In figure 13, we have plotted as in figure 10, the quantity $|x_{\parallel}|^{5/12} \sqrt{r} |\mathbf{v}|$ versus x_{\parallel} , which is still expected to be provided by (4.24). As previously, we do observe a good agreement between theoretical predictions and numerical results.

5. Discussion

We have shown that the internal shear layers created by the libration of a convex object can be described by the similarity solutions introduced by Moore & Saffman (1969). We have provided the amplitude and the parameter controlling the form of

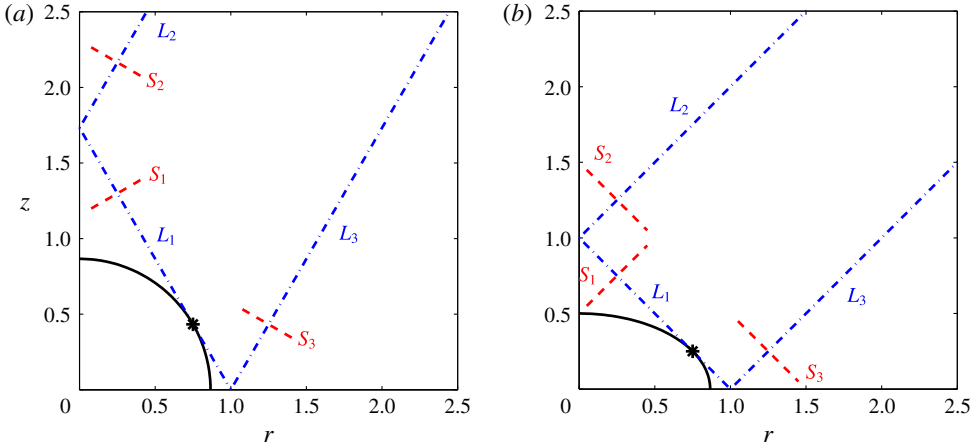


FIGURE 11. (Colour online) Definition of the characteristic lines and sections for a librating spheroid. (a) Sphere of radius $\sqrt{3}/2$ for $\omega = 1$. (b) Oblate spheroid of eccentricity $\sqrt{2/3}$ for $\omega = \sqrt{2}$.

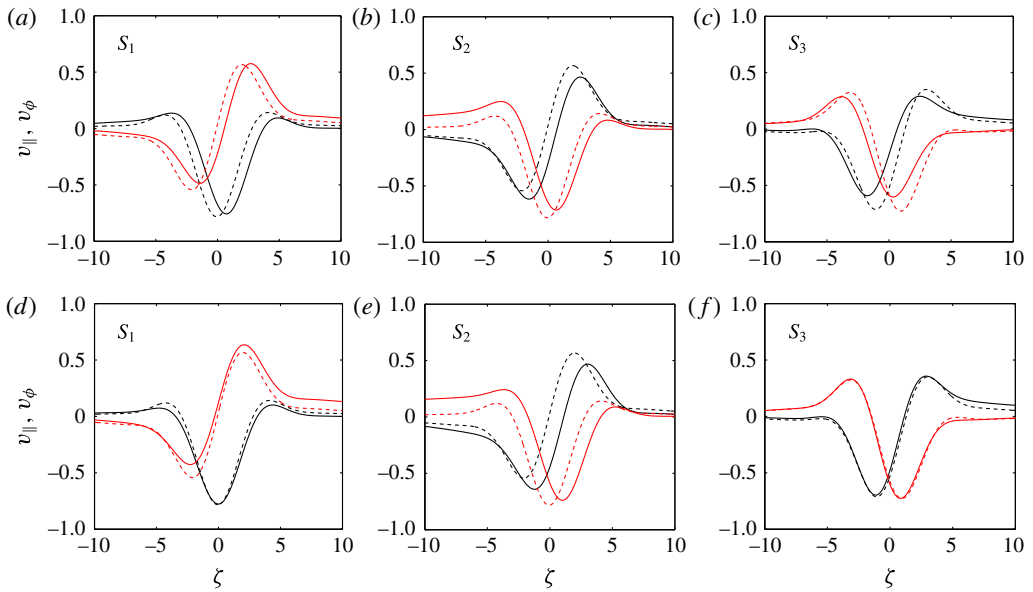


FIGURE 12. (Colour online) Same as figure 9 across the sections defined in figure 11. (a–c) Sphere with $\omega = 1$; (d–f) oblate spheroid of eccentricity $\sqrt{2/3}$ with $\omega = \sqrt{2}$. For both cases, $\varepsilon = 10^{-4}$, $E_s = 10^{-5}$ (i.e. $E = 1.78 \times 10^{-5}$) and $t = 508.9\pi/\omega$.

the solution for a disk and for any smooth object. For a smooth object, we have in particular shown that the amplitude is proportional to the local curvature radius at the power 1/4 at the critical latitude where the internal shear layers are emitted. Interestingly, we have also obtained that this amplitude is larger for a smooth object (with a scaling in $E^{1/12}$) than for a disk (with a scaling in $E^{1/6}$). The consequence of this larger amplitude in the internal shear layers is an even larger amplitude in $E^{-1/12}$

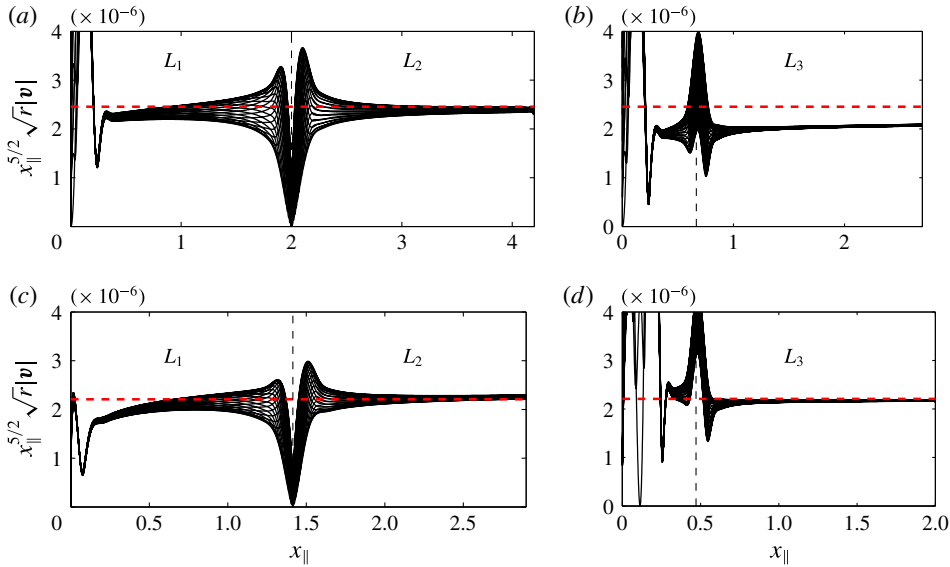


FIGURE 13. (Colour online) Same as figure 10 for the configurations defined in figure 11. (a,b) Sphere with $\omega = 1$; (c,d) oblate spheroid of eccentricity $\sqrt{2/3}$ with $\omega = \sqrt{2}$. For both cases, $\varepsilon = 10^{-4}$ and $E_s = 10^{-5}$ (i.e. $E = 1.78 \times 10^{-5}$).

at the point of focus on the axis (see appendix A). At this particular point on the axis, the solution therefore grows and diverges as $E \rightarrow 0$, clearly demonstrating the singular character of the solution in this limit.

The scaling in $E^{1/12}$ for the velocity amplitude in the internal shear layers is larger than that reported in the literature (e.g. Kerswell 1995; Calkins *et al.* 2010). As a consequence, the zonal flow created by the self-interaction of the harmonic solution is also expected to be larger. Following the analysis performed in Le Dizès (2015), we can expect a zonal flow in $\varepsilon^2 E^{1/6}$ in the internal shear layers and in $\varepsilon^2 E^{-1/2}$ at the focus point on the axis. This last scaling implies that the nonlinear corrections become large as soon as ε reaches $E^{1/4}$, that is well before the linear solution has reached an amplitude of order 1.

For illustrating the geophysical relevance of our results, let us consider two examples: the liquid core of Mercury and the subsurface ocean of Enceladus, whose existences have been demonstrated by studies of their surface librating motions (Margot *et al.* 2007; Thomas *et al.* 2016). Relevant physical parameters are listed in table 1. Using our scaling law (4.24), typical velocities within internal shear layers are 1.3×10^{-6} and 1.6×10^{-4} m s⁻¹, while estimates for the zonal flow at the focus point give 2.0×10^{-2} and 6.3 m s⁻¹. For comparison, typical velocities in the Earth’s core related to the convective dynamo are 10^{-4} m s⁻¹ (Gubbins & Roberts 1987) and typical tidal speeds in the Earth’s oceans are 3×10^{-2} m s⁻¹ (St Laurent & Garrett 2002). The influence of the fluid motions described here on planetary dynamics, for instance through magnetic field generation and energy dissipation, should thus be taken into account.

We have only considered internal shear layers created by libration of an axisymmetric object, hence created by viscous coupling. This forcing is weak as it is actually associated with an oscillating Ekman pumping of order $E^{1/2}$. A larger forcing is

	Ω^* (rad s ⁻¹)	r^* (km)	ω	ε	E
Mercury	1.2×10^{-6}	1000 (from 0–1700)	2/3	1.3×10^{-4}	8×10^{-13}
Enceladus	5.2×10^{-5}	200	1	2.1×10^{-3}	5×10^{-13}

TABLE 1. Physical parameters for the librating motion of the liquid core of Mercury (Margot *et al.* 2007; Noir *et al.* 2009) and the subsurface ocean of Enceladus (Thomas *et al.* 2016). In both cases, we consider a typical viscosity $\nu = 10^{-6}$ m² s⁻¹, which is supposedly representative of both water/salty water in oceans and liquid iron in planetary cores (see e.g. de Wijs *et al.* 1998).

obtained when it is generated by pressure forces. For example, if the object was oscillated vertically or horizontally, or when the librating object is non-axisymmetric, as in tidally deformed planetary bodies, a much larger amplitude would have been obtained. This situation has been analysed in several works in the context of stratified fluids (e.g. Mowbray & Rarity 1967). In these cases, internal shear layers have also been observed and described by the same family of similarity solutions in the far field (e.g. Thomas & Stevenson 1972; Hurley & Keady 1997; Flynn, Onu & Sutherland 2003; Voisin 2003). It would be interesting to determine whether the present approach can be also used to characterize the near field.

It is finally worth emphasizing that we have considered an open domain only. In a closed geometry such as a spherical shell, the internal shear layers are reflected on the boundaries. This implies that they can interact with themselves after a finite number of reflections modifying their internal structure. Such a modification was already quantified a long time ago for the stationary flow generated between two differentially rotating spheres by Stewartson (1966), who showed that the structure of the internal shear layer becomes more complex with nested regions of widths $E^{1/3}$, $E^{2/7}$ and $E^{1/4}$. We can imagine that similar complications would occur for the librating case if the internal shear layer would form a closed circuit.

Acknowledgements

This work received support from the French Agence Nationale de la Recherche under the A*MIDEX grant ANR-11-IDEX-0001-02, the LABEX MEC project ANR-11-LABX-0092 and the ANR LIPSTIC project ANR-13-JS05-0004-01.

Appendix A. Local asymptotic solution for the internal shear layer close to the axis

The similarity solution diverges as r goes to zero. A new expression has to be obtained close to the axis. For this purpose, we can use the general expression in terms of the Hankel transform

$$v_r = \int_0^\infty U(k) J_1(kr) e^{i\mu_1 z} dk, \quad (\text{A } 1a)$$

$$v_\phi = \int_0^\infty V(k) J_1(kr) e^{i\mu_1 z} dk, \quad (\text{A } 1b)$$

$$v_z = \int_0^\infty W(k) J_0(kr) e^{i\mu_1 z} dk, \quad (\text{A } 1c)$$

$$p = \int_0^\infty P(k)J_0(kr)e^{i\mu_1 z} dk, \tag{A 1d}$$

where μ_1 is the ‘non-viscous’ wavenumber, which expands, when $E \rightarrow 0$, as

$$\mu_1 \sim k \frac{\cos \theta_c}{\sin \theta_c} \left(1 + iE \frac{k^2}{2 \cos \theta_c \sin^4 \theta_c} \right). \tag{A 2}$$

At leading order, the amplitudes U , V , W and P are related with each other by the relations (see Le Dizès 2015)

$$W = i \frac{\sin \theta_c}{\cos \theta_c} U, \tag{A 3a}$$

$$U = i \cos \theta_c V, \tag{A 3b}$$

$$kP = -2V - 2i \cos \theta_c U = -2 \sin \theta_c V. \tag{A 3c}$$

Introducing the local variables

$$\tilde{r} = r/E^{1/3}, \quad \tilde{z} = (z - \sin \theta_c)/E^{1/3}, \tag{A 4a,b}$$

(A 1a–d) can be written as

$$v_r = i \cos \theta_c \int_0^\infty \tilde{V}J_1(\tilde{k}\tilde{r})e^{i\tilde{k} \cotan \theta_c \tilde{z}} d\tilde{k}, \tag{A 5a}$$

$$v_\phi = \int_0^\infty \tilde{V}J_1(\tilde{k}\tilde{r})e^{i\tilde{k} \cotan \theta_c \tilde{z}} d\tilde{k}, \tag{A 5b}$$

$$v_z = -\sin \theta_c \int_0^\infty \tilde{V}J_0(\tilde{k}\tilde{r})e^{i\tilde{k} \cotan \theta_c \tilde{z}} d\tilde{k}, \tag{A 5c}$$

$$p = -2 \sin \theta_c E^{1/3} \int_0^\infty \tilde{V} \frac{J_0(\tilde{k}\tilde{r})}{\tilde{k}} e^{i\tilde{k} \cotan \theta_c \tilde{z}} d\tilde{k}. \tag{A 5d}$$

The expression of \tilde{V} is obtained by matching these expressions with the similarity solution on L_1 . When both \tilde{z} and \tilde{r} go to infinity, equation (A 5b) for v_ϕ can be written as

$$v_\phi \sim \sqrt{\frac{1}{2\pi\tilde{r}}} \int_0^\infty \frac{\tilde{V}}{\sqrt{\tilde{k}}} (e^{i\tilde{k}(\tilde{r} + \cotan \theta_c \tilde{z}) - 3i\pi/4} + e^{i\tilde{k}(-\tilde{r} + \cotan \theta_c \tilde{z}) + 3i\pi/4}) d\tilde{k}, \tag{A 6}$$

using the expansion of the Bessel function J_1 at infinity. If we now assume that

$$\tilde{V} = E^{-1/6} C_0 \frac{\sqrt{2\pi\tilde{k}}^{m-1/2}}{(m-1)! \sin^m \theta_c} e^{-\tilde{k}^3/(2 \cos \theta_c \sin^4 \theta_c)} e^{5i\pi/4 - im\pi/2}, \tag{A 7}$$

this expression becomes

$$v_\phi \sim \frac{1}{\sqrt{\tilde{r}}} (iC_0 H_m(1/\cos \theta_c, \zeta^{(1)}) + C_0 H_m(1/\cos \theta_c, \zeta^{(2)})), \tag{A 8}$$

where $\zeta^{(1)}$ and $\zeta^{(2)}$ are the similarity variables close to the axis along L_1 and L_2 respectively:

$$\zeta^{(1)} = (2 \sin \theta_c \cos \theta_c)^{1/3} (\sin \theta_c \tilde{r} + \cos \theta_c \tilde{z}), \tag{A 9a}$$

$$\zeta^{(2)} = (2 \sin \theta_c \cos \theta_c)^{1/3} (-\sin \theta_c \tilde{r} + \cos \theta_c \tilde{z}). \tag{A 9b}$$

The first term in (A 8) is exactly the expression of the azimuthal velocity component of the similarity solution along L_1 close to $x_{\parallel} = 1/\cos\theta_c$ (see expressions (2.8) and (2.15)). The second term corresponds to the similarity solution along L_2 . It shows that the azimuthal velocity component of the similarity solution keeps the same amplitude but with a phase shift of $-\pi/2$. Along L_2 , the expressions (2.10) and (2.15) for $v_{\parallel}^{(0)}$ and $v_{\phi}^{(0)}$ have thus to be replaced by

$$v_{\parallel}^{(0)} = iC_0H_m(x_{\parallel}, \zeta), \quad v_{\phi}^{(0)} = C_0H_m(x_{\parallel}, \zeta), \quad (\text{A } 10a,b)$$

where x_{\parallel} starts at the value $1/\cos\theta_c$ from the point $(0, \tan\theta_c)$ on the z axis.

In the $O(E^{1/3})$ neighbourhood around the focus point, the solution is given by (A 5a–d) with \tilde{V} and C_0 provided by (A 7) and (4.20b), respectively. In particular, this implies that the three velocity components become of order $E^{-1/12}$ close to the focus point.

REFERENCES

- ALDRIDGE, K. D. & TOOMRE, A. 1969 Axisymmetric inertial oscillations of a fluid in a rotating spherical container. *J. Fluid Mech.* **37**, 307–323.
- CALKINS, M. A., NOIR, J., ELDREDGE, J. D. & AURNOU, J. M. 2010 Axisymmetric simulations of libration-driven fluid dynamics in a spherical shell geometry. *Phys. Fluids* **22**, 086602.
- CÉBRON, D., LE BARS, M., MOUTOU, C. & LE GAL, P. 2012 Elliptical instability in terrestrial planets and moons. *Astron. Astrophys.* **539**, A78.
- FLYNN, M. R., ONU, K. & SUTHERLAND, B. R. 2003 Internal wave excitation by a vertically oscillating sphere. *J. Fluid Mech.* **494**, 65–93.
- GREENSPAN, H. P. 1968 *The Theory of Rotating Fluids*. Cambridge University Press.
- GUBBINS, D. & ROBERTS, P. H. 1987 Magnetohydrodynamics of the Earth's core. *Geomagnetism* **2**, 1–183.
- HURLEY, D. G. & KEADY, G. 1997 The generation of internal waves by vibrating elliptic cylinders. Part 2: approximate viscous solution. *J. Fluid Mech.* **351**, 119–138.
- KERSWELL, R. 1995 On the internal shear layers spawned by the critical regions in oscillatory Ekman boundary layers. *J. Fluid Mech.* **298**, 311–325.
- KIDA, S. 2011 Steady flow in a rapidly rotating sphere with weak precession. *J. Fluid Mech.* **680**, 150–193.
- KLEIN, M., SEELIG, T., KURGANSKY, M., GHASEMI, V. A., BORCIA, I. D., WILL, A., SCHALLER, E., EGBERS, C. & HARLANDER, U. 2014 Inertial wave excitation and focusing in a liquid bounded by a frustrum and a cylinder. *J. Fluid Mech.* **751**, 255–297.
- KOCH, S., HARLANDER, U., EGBERS, C. & HOLLERBACH, R. 2013 Inertial waves in a spherical shell induced by librations of the inner sphere: experimental and numerical results. *Fluid Dyn. Res.* **45** (3), 035504.
- LE BARS, M., CÉBRON, D. & LE GAL, P. 2015 Flows driven by libration, precession, and tides. *Annu. Rev. Fluid Mech.* **47**, 163–193.
- LE DIZÈS, S. 2015 Wave field and zonal flow of a librating disk. *J. Fluid Mech.* **782**, 178–208.
- MACHICOANE, N., CORTET, P.-P., VOISIN, B. & MOISY, F. 2015 Influence of the multipole order of the source on the decay of an inertial wave beam in a rotating fluid. *Phys. Fluids* **27**, 066602.
- MARCOTTE, F., DORMY, E. & SOWARD, A. 2016 On the equatorial Ekman layer. *J. Fluid Mech.* **803**, 395–435.
- MARGOT, J.-L., PEALE, S. J., JURGENS, R. F., SLADE, M. A. & HOLIN, I. V. 2007 Large longitude libration of mercury reveals a molten core. *Science* **316** (5825), 710–714.
- MCEWAN, A. D. 1970 Inertial oscillations in a rotating fluid cylinder. *J. Fluid Mech.* **40**, 603–640.

- MOORE, D. W. & SAFFMAN, P. G. 1969 The structure of free vertical shear layers in a rotating fluid and the motion produced by a slowly rising body. *Phil. Trans. R. Soc. Lond. A* **264**, 597–634.
- MOWBRAY, D. E. & RARITY, B. S. H. 1967 A theoretical and experimental investigation of the phase configuration of internal waves of small amplitude in a density stratified liquid. *J. Fluid Mech.* **28**, 1–16.
- NOIR, J., HEMMERLIN, F., WICHT, J., BACA, S. M. & AURNOU, J. M. 2009 An experimental and numerical study of librational driven flow in planetary cores and subsurface oceans. *Phys. Earth Planet. Inter.* **173** (1), 141–152.
- OGILVIE, G. I. 2005 Wave attractors and the asymptotic dissipation rate of tidal disturbances. *J. Fluid Mech.* **543**, 19–44.
- PEAT, K. S. 1978 Internal and inertial waves in a viscous rotating stratified fluid. *Appl. Sci. Res.* **33**, 481–499.
- PROUDMAN, I. 1956 The almost-rigid rotation of viscous fluid between concentric spheres. *J. Fluid Mech.* **1**, 505–516.
- RIEUTORD, M., GEORGEOT, B. & VALDETTARO, L. 2001 Inertial waves in a rotating spherical shell: attractors and asymptotic spectrum. *J. Fluid Mech.* **435**, 103–144.
- RIEUTORD, M. & VALDETTARO, L. 1997 Inertial waves in a rotating spherical shell. *J. Fluid Mech.* **341**, 77–99.
- ROBERTS, P. H. & STEWARTSON, K. 1963 On the stability of a MacLaurin spheroid of small viscosity. *Astrophys. J.* **137**, 777–790.
- ST LAURENT, L. & GARRETT, C. 2002 The role of internal tides in mixing the deep ocean. *J. Phys. Oceanogr.* **32** (10), 2882–2899.
- STEVENSON, T. N., BEARON, J. N. & THOMAS, N. H. 1974 An internal wave in a viscous heat-conducting isothermal atmosphere. *J. Fluid Mech.* **65**, 315–323.
- STEWARTSON, K. 1957 On almost rigid rotations. *J. Fluid Mech.* **3**, 17–26.
- STEWARTSON, K. 1966 On almost rigid rotations. Part 2. *J. Fluid Mech.* **26**, 131–144.
- THOMAS, N. H. & STEVENSON, T. N. 1972 A similarity solution for viscous internal waves. *J. Fluid Mech.* **54**, 495–506.
- THOMAS, P. C., TAJEDDINE, R., TISCARENO, M. S., BURNS, J. A., JOSEPH, J., LOREDO, T. J., HELFENSTEIN, P. & PORCO, C. 2016 Enceladus's measured physical libration requires a global subsurface ocean. *Icarus* **264**, 37–47.
- TILGNER, A. 2000 Oscillatory shear layers in source driven flows in an unbounded rotating fluid. *Phys. Fluids* **12**, 1101–1111.
- VOISIN, B. 2003 Limit states of internal wave beams. *J. Fluid Mech.* **496**, 243–293.
- VAN DE VOOREN, A. I. 1992 The Stewartson layer of a rotating disk of finite radius. *J. Engng Maths* **26**, 131–152.
- WALTON, I. C. 1975 On waves in a thin rotating spherical shell of slightly viscous fluid. *Mathematika* **22**, 46–59.
- DE WIJS, G. A., KRESSE, G., VOCADLO, L., DOBSON, D. *et al.* 1998 The viscosity of liquid iron at the physical conditions of the earth's core. *Nature* **392** (6678), 805.
- ZHANG, K., CHAN, K. H., LIAO, X. & AURNOU, J. M. 2013 The non-resonant response of fluid in a rapidly rotating sphere undergoing longitudinal libration. *J. Fluid Mech.* **720**, 212.